Influence of alloy composition on the tribomechanical properties of 50% blend of CoCrWMoCFeNiSiMn (stellite 1) and CoCrMoCFeNiSiMn (stellite 21) alloys.

AHMED, R., KUMAR, V., FAISAL, N.H., MARRI, M. and DAVIES, S.

2025

JMEPEG
https://doi.org/10.1007/s11665-025-11034-7

1059-9495/$19.00

ORIGINAL RESEARCH ARTICLE

Influence of Alloy Composition on the Tribomechanical Properties of 50% Blend of CoCrWMoCFeNiSiMn (Stellite 1) and CoCrMoCFeNiSiMn (Stellite 21) Alloys

R. Ahmed, V. Kumar, N.H. Faisal, M. Marri, and S. Davies

Submitted: 6 September 2024 / Revised: 23 November 2024 / Accepted: 17 December 2024

This paper aims to investigate the structure–property relationship of the blend of two different carbide-type wear resistance Stellite® alloys, i.e., high-carbon and high-tungsten CoCrWMoCFeNiSiMn (Stellite 1) alloy and high-molybdenum CoCrMoCFeNiSiMn (Stellite 21) alloy. Blended alloys can be tailored to specific tribomechanical properties that cannot be achieved using standard pre-alloyed powders. Gas-atomized powders were HIPed (hot isostatically pressed) in an argon environment for 4 h at a temperature and pressure of 1200 °C and 100 MPa, respectively. The microstructure of the alloys was investigated using X-ray diffraction (XRD) and scanning electron microscopy (SEM). Micro-hardness, macro-hardness (HV), tensile and Charpy impact tests were performed to characterize the mechanical properties. Wear properties were investigated using dry sand rubber wheel (DSRW), self-mated pin-on-disk (PoD) and ball-on-flat (BoF) tests. Relationships between the chemical composition of the alloys and total carbide fraction (TCF), hardness, yield strength and Charpy impact energy (E_c) were investigated. Structure–property relationships are developed between the wear rate and chemical composition via mechanical properties. Wear mechanisms are discussed based on phase composition and alloy microstructure. The wear performance was more dominated by relationship $\left(\frac{TCF \times HV}{E_c}\right)$. Mathematical relationships of wear rate are developed which can be applied to both CoCrW and CoCrWMo alloy blends.

Keywords blending, cobalt alloys, HIPing, mechanical properties, sliding wear, stellite alloys, structure–property relationship

1. Introduction

The structure–property relationship of wear-resistant ternary Co-based alloys, also known as Stellite® alloys, is dependent not only on the alloy composition but also on the manufacturing process and tribological conditions (Ref 1-4). For general wear-resistant applications in moderately corrosive environments up to a temperature of 600 °C, CoCrWMoCFeNiSiMn alloys such as Stellite 6, 1 and 20 are commonly used. For severe corrosive environments such as acids (HCl, H_2SO_4) and seawater, CoCrMoCFeNiSiMn alloys such as Stellite 21 are preferred. The atomic weight of Mo is roughly half of W, enabling twice the number of Mo elements in the CoCr matrix for the same wt% composition. Replacing W with Mo improves the alloy performance in a Cl^- ion environment. New alloy compositions containing both W and Mo can be explored by

R. Ahmed, V. Kumar, and **M. Marri**, School of Engineering and Physical Sciences, Heriot-Watt University, Edinburgh EH14 4AS, UK; **N.H. Faisal**, School of Engineering, Robert Gordon University, Aberdeen AB10 7GJ, UK; and **S. Davies**, Bodycote HIP Ltd, Sheffield Road, Sheepbridge, Chesterfield S41 9ED, UK. Contact e-mail: R.Ahmed@hw.ac.uk.

List of Symbols

BSE	Backscattered electron image
C_w	Tungsten content (%)
C_c	Carbon content (%)
CoCrW	Stellite 1 (CoCrWMoCFeNiSiMn)
CoCrMo	Stellite 21 (CoCrMoCFeNiSiMn)
$E_{\%}$	Tensile elongation (%)
E_c	Charpy impact energy (J)
EDS	Energy dispersive spectroscopy
FCC	Face-centered cubic
HCP	Hexagonal close-packed
ML	Machine learning
P1	HIPed stellite 1
P2	HIPed blend
P3	HIPed stellite 21
P_m	Hertz contact pressure (GPa)
R_{cwm}	Relative C, W and Mo content (%)
S_{wm}	Sum of W and Mo (%)
SFE	Stacking faulty energy
SE	Secondary electron image
TCF	Total carbide fraction (%)
UTS	Ultimate tensile strength (MPa)
W_{DSRW}	Wear rate in DSRW tests (mm^3/N m)
W_{PoD}	Wear rate in pin-on-disk tests (mm^3/N m)
W_{BoF}	Wear rate in ball-on-flat tests (mm^3/N m)
σ_y	Yield strength (MPa)

Published online: 24 March 2025

blending CoCrWMoCFeNiSiMn and CoCrMoCFeNiSiMn alloys.

Stellite 1 is a high-carbon and high-tungsten CoCrWMoCFeNiSiMn alloy, making it suitable for tribological applications such as valve seating, wear pads in gas turbines, bearing sleeves, slurry pumps, ball bearings and expeller screws. Stellite 1 alloy is labeled as CoCrW alloy in this paper. Stellite 21 is a low-carbon, high-molybdenum alloy used in applications such as forging and hot-stamping dies and valve trims in the chemical industry (Ref 1, 2). Stellite 21 alloy is labeled as CoCrMo alloy in this paper. The applications of these alloys rely on the excellent integration of mechanical and tribological properties, providing a combination of hardness, toughness and strength to combat erosion, corrosion, cavitation, sliding and abrasive wear in a temperature range up to 760 °C (Ref 1-3). Casting (Ref 1-4), power metallurgy such as HIPing (hot isostatic pressing) (Ref 4) and re-HIPing (Ref 5), coatings (Ref 6), blending (Ref 7), laser cladding and hard facing (8), plasma sintering (Ref 9) and additive manufacturing (3D printing) (Ref 10) are some of the commonly used techniques used to manufacture these alloys.

The wear resistance of Stellite alloys benefits from the strain-induced face-centered cubic (FCC) to hexagonal close-packed (HCP) transformation of Co (Ref 11, 12), solid solution strengthening (e.g., Co_3W, Co_7W_6, Co_3Mo, Co_2Mo_3, Co_7Mo_6) in the ternary matrix alloy due to varying amounts of W or Mo, Cr, Co, Mn, Fe, Si and other elements, and Cr-, W- or Mo-rich carbides (M_6C, $M_{12}C$, M_7C_3, $M_{23}C_7$) (Ref 11-16). The shape, size and composition of these carbides, and thus, their structure–property relationship depend upon the alloy's manufacturing process and chemical composition (Ref 2-16). Prediction of Stellite alloys' wear performance has also been attempted using mathematical (Ref 17) and numerical modeling techniques (Ref 18).

Blending of Stellite alloys is a recent development in the published literature (Ref 7, 19). This technique allows the designer to tailor the blended alloy to a required composition to suit structure–property and tribomechanical properties. Blending can involve two or more alloy powders, and the proportion of these blends can vary depending on the application. Additive manufacturing (Ref 10) can also offer a range of possible alloy combinations through blending, e.g., either via the use of blended powders or by feeding individual alloy powders through multiple feeders to print composite material components. Regardless of the manufacturing route, developing these alloy blends requires further research to provide an understanding of the structure–property relationship linking them to tribomechanical performance. Such understanding also needs to be underpinned by mathematical and numerical models (Ref 17, 18) for alloy development and prediction of tribomechanical properties based on elemental composition (Ref 20). Recent developments in alloy design are beginning to explore these concepts, where a new knowledge-based framework is used to tailor compositionally complex materials (CCMs, both alloys and ceramics) using different manufacturing techniques, with the required combination of tribomechanical properties (Ref 7, 19, 20).

Blending of CoCrW alloys to simultaneously vary the C, Cr and W content has previously been attempted (Ref 7). However, by switching W with Mo in the Stellite alloy system, e.g., in Stellite 21 (Ref 21-23) and Stellite 22 (Ref 21), the carbide formation and solid solution strengthening change, affecting the tribomechanical performance. The mechanical properties of W-rich and Mo-rich carbides differ, and the atomic weight differences between these two alloying elements change the diffusion kinetics for intermetallic compounds. The aim of the current investigation was, therefore, to form a new CoCrWMo alloy by blending a high-carbon and high-tungsten CoCrW (Stellite 1) and a low-carbon high-molybdenum CoCrMo alloy (Stellite 21) and investigate its tribomechanical properties and structure–property relationship. The results of this investigation are also compared with the earlier investigation of the CoCrW blend (Ref 7) to aid the discussion and understand the influence of alloy composition changes on the structure–property relationship. The research questions addressed in this paper are to (1) understand the failure mechanism and wear performance of the CoCrW + CoCrMo blend and (2) improve the existing mathematical models for predictions of wear performance in CoCrW + CoCrMo blends. The tribomechanical properties of these alloys are composition-dependent. There is no investigation in the published literature that considers the tribomechanical properties of a blend of a high C and W (Stellite 1) with low C and high Mo (Stellite 21). The novelty of this work lies in not only understanding the influence of this unique blending on the tribomechanical properties, but also modifying the existing mathematical model of the structure–property relationship developed earlier for high-W + C alloys (Ref 7) to include a high-Mo alloy composition of the blend. Hence, the improved mathematical model will not only apply to high-W + C alloy blend, e.g., Stellite 6 and 20, but also to W + Mo + C alloy blends (Stellite 1 and 21). Apart from (Ref 7) and (Ref 19), no investigation in the published literature has attempted the blending of Stellite alloys. In summary, not only there is the literature on blended Stellite alloys limited, but there is no literature on blended CoCrW + Mo alloys.

2. Experimental

2.1 Materials and Microstructure

Gas-atomized powders of chemical composition similar to base alloys of Stellite 1 (P1) and Stellite 21 (P3), shown in Fig. 1, were used to manufacture a 50:50 blend alloy (P2). Blending was done by tumbling the two powders in a powder hopper before HIPing, using industrially optimized parameters. The chemical composition of the base alloys (P1, P3) and the blended alloy (P2) is summarized in Table 1. These materials were manufactured by Deloro Stellite (UK) using industrially optimized parameters. Table 2 provides the sieve analysis of the base alloys (P1, P3). The alloys were manufactured from the powders using HIPing (Hot isostatic pressing) for 4 hours at a temperature and pressure of 1200 °C and 100 MPa, respectively.

The microstructure of the alloys was investigated using scanning electron microscopy (SEM) in secondary (SE) and backscattered (BSE) electron modes. X-ray diffraction (XRD) with Cu-Kα radiation (λ = 1.5406 Å) was used to identify microstructural components in the alloys. ImageJ was used to evaluate the area fraction of the carbide and matrix components.

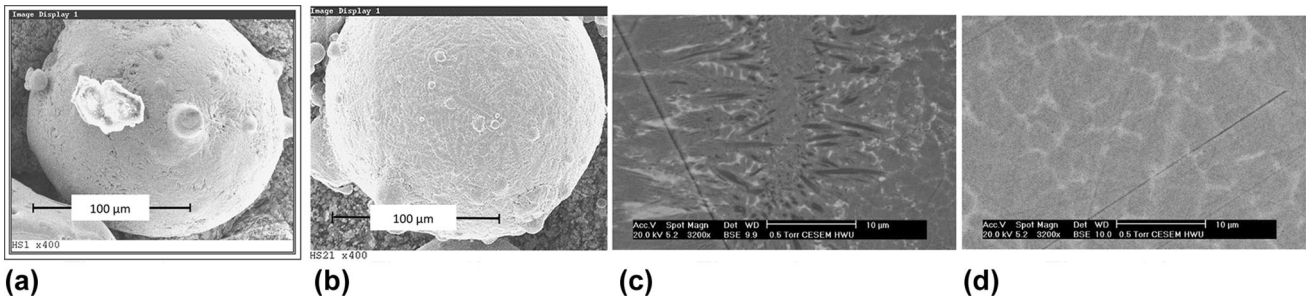

Fig. 1 Surface morphology of (a) Stellite 1 (P1), (b) Stellite 21 (P3) powders and (c, d) SEM observations of powder cross sections of P1, P3, respectively

Table 1 Chemical compositions of the base and blended HIPed Stellite CoCrWMo alloys (in wt.%)

Stellite	Co	Cr	W	Mo	C	Fe	Ni	Si	Mn
P1 (Stellite 1)	Bal.	31.70	12.70	0.29	2.47	2.30	2.38	1.06	0.26
P2 (50:50 blend of P1 and P3)	Bal.	29.75	6.35	2.90	1.38	1.93	2.56	1.36	0.54
P3 (Stellite 21)	Bal.	27.80	0.00	5.50	0.28	1.55	2.74	1.66	0.82

Table 2 Sieve analysis of the base Stellite powders (in wt.%)

Stellite powder	+ 250, μm	+ 180, μm	+ 125, μm	+ 45, μm	− 45, μm
P1 (Stellite 1)	0.10 + 38, μm	2.40 + 20, μm	47.90 − 20, μm	49.50	0.10
P3 (Stellite 21)	0.00	50.50	49.50		

2.2 Hardness, Tensile and Impact Toughness Tests

Micro-hardness and macro-hardness measurements were taken at a load of 2.94 and 294 N, respectively, using a Mitutoyo (MVK-H1) and Avery hardness tester. An average of five macro-hardness and ten micro-hardness measurements are reported in the results section. An Instron machine was used to conduct tensile tests following the BS EN 10002 standard. Unnotched Charpy impact tests were performed on samples with dimensions of 10 × 10 × 55 mm, using an Avery Charpy impact tester at an impact rate of 5 m/s. An average of three values are reported for tensile and impact test results.

2.3 DSRW Abrasive Wear Tests

Dry sand rubber wheel (DSRW) abrasion tests were performed at a load of 130 N using Procedure B of the ASTM G65 standard. A polyurethane rim wheel of 228.6 mm with a hardness of Shore A-60 was used at a speed of 200 ± 5 rpm to conduct DSRW tests. Each test was performed for 2000 revolutions. Two types of silica sand particles labeled as sand A (85 wt.% particles had sizes in the range of 90−180 μm) and B (85 wt.% particles having sizes in the range of 150–300 μm) were used as abrasives at a flow rate of 330 g/min. Wear mass loss was measured using a precision balance to an accuracy of 0.001 g. Wear volume loss was calculated from the mass loss and density of alloys. Three tests were conducted with each sand, and averaged values are reported in the results section.

2.4 Sliding Wear Tests

Sliding wear tests were conducted following ASTM G133-02 in two different reciprocating configurations of pin-on-disk and ball-on-flat. Pin-on-disk (PoD) tests were self-mated, whereas a sintered WC-Co ball with a radius of 6.35 mm was used as a counterbody for the ball-on-flat (BoF) tests. Figure 2 shows the schematic representation of the test apparatus for PoD and BoF tests. In this arrangement, the sliding motion of the test sample contacting either a ball or pin was controlled through the motor controller. The tension–compression load cell provided the friction force measurement during the test. Data acquisition and the LabVIEW program enabled the recording of test variables. Table 3 summarizes the sliding wear parameters used in the current investigation. A ZYGO NewView interferometer was used to evaluate the wear volume loss. Averaged values of three tests are reported in the results section.

3. Results

3.1 Microstructure

Figure 3 shows the microstructure of the base and blended alloys. HIPed Stellite 1 (P1) is a relatively high-carbon CoCrW alloy, with Cr- and W-rich carbides in the CoCrW solid solution matrix (Fig. 3a). HIPed Stellite 21 (P3) is a low-carbon CoCrMo alloy, with only a few carbides in the matrix (Fig. 3d).

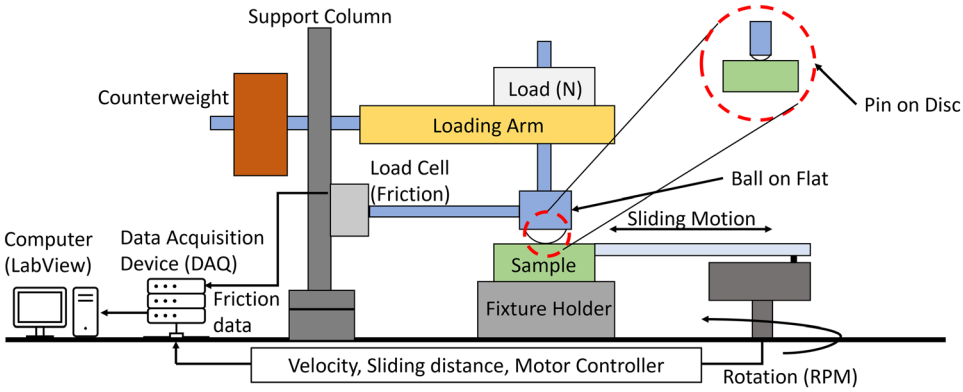

Fig. 2 Schematic representation of the arrangement for ball-on-flat and pin-on-disk tests

Table 3 Sliding wear parameters for reciprocating pin-on-disk and ball-on-flat tests

Test method	Pin-on-disk	Ball-on-flat
Load (N)	25	25
Stroke length (mm)	10	10
Sliding frequency (Hz)	5	1
Sliding distance (m)	100	500
Counterbody	Self-mated pin of 10 mm tip radius	Sintered WC-5 wt.%Co
Mean Hertzian Pressure (P_m) (GPa)	0.62	1.1

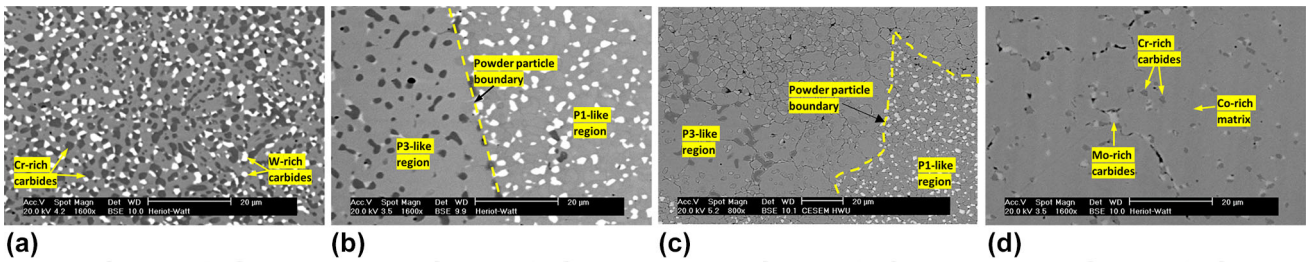

Fig. 3 SEM observations of HIPed Stellite alloy (a) P1 (Stellite 1); (b, c) P2 (50:50 blend of P1 and P2); (d) P3 (Stellite 21)

The blending of the CoCrW alloy (Stellite 1, P1) and the CoCrMo alloy (Stellite 21, P3) resulted in a microstructure with Cr-rich (dark phase), W-rich (light phase) and Mo-rich carbides (light phase) coexisting in the Co-rich matrix (Fig. 3b). Fig. 3(c) shows the powder particle boundary of Stellite 1 and 21 at a lower magnification, highlighting the shape after deformation of near-spherical powders during HIPing. The average powder particle size of Stellite 1 was larger ($\simeq$ 125 to 45 μm) than that of Stellite 21 ($\simeq$ 38 to 20 μm), as summarized in Table 2. Despite this difference in powder particle size, this figure shows complete consolidation between the two powders with no porosity at the powder particle interface under the HIPing conditions used in this work. The XRD spectra for these alloys are shown in Fig. 4. The image analysis results of these blends are summarized in Table 4.

3.2 Mechanical Tests

The mechanical properties of the base and blended alloys are shown in Table 5. The HIPed Stellite 21 alloy (P3) had the lowest hardness and yield strength and the highest elongation and Charpy impact energy. Figure 5 shows the SEM fractographs of the fractured alloys after the tensile and Charpy impact tests.

3.3 Abrasive Wear Tests

Figure 6 shows the results of the abrasive wear test results. Averaged results are presented in terms of volume loss and wear rate obtained from normal load and sliding distance. The figure also shows the standard deviation of the test data. The volume loss of the CoCrMo Stellite 21 alloy (P3) was much higher than that of the HIPed blend (P2). Figure 7 shows the SEM observations of the wear scars. These observations indicate plowing of the softer metal matrix against the harder silica sand particles, carbide pullout due to sliding of sand particles against harder carbides, carbide fracture due to the loading of sand particles on carbide surfaces and presence of oxidized film, as described later in the discussion section.

3.4 Sliding Wear Tests

Figure 8 summarizes the sliding wear results for PoD and BoF tests. Both pin and disk wear rates are summarized for the

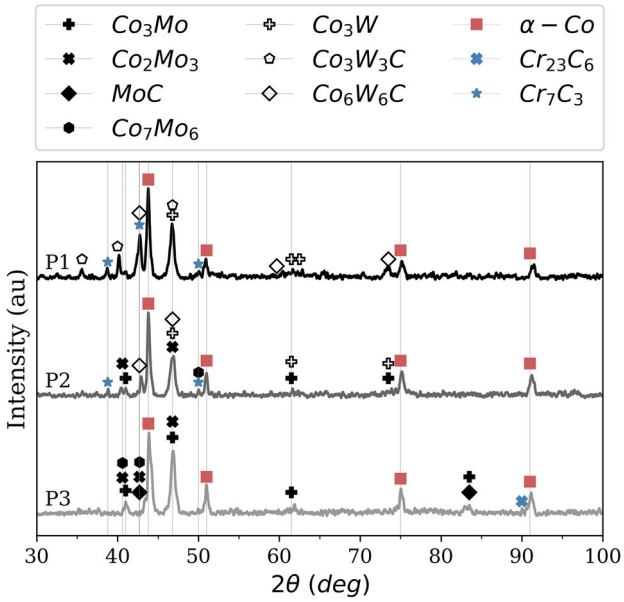

Fig. 4 XRD spectra of HIPed Stellite alloys (a) P1 (Stellite 1), (b) P2 (50:50 blend of P1 and P2), (c) P3 (Stellite 21)

PoD test. Averaged values of wear volume loss and wear rate, along with the standard deviation of the experimental data, are presented in this figure. There was negligible wear on the WC-Co ball for the BoF test; hence, only wear rates for the disk are summarized in the figure. SEM observations of the wear scars for these tests are shown in Fig. 9. This figure shows that carbide pullout due to asperity interaction, plowing of softer matrix by asperities and wear debris, the embedding of wear debris on the worn surface and oxidized film were the dominant wear mechanisms, as described later in the discussion section.

4. Discussion

4.1 Microstructure

Stellite 1 (P1) was a CoCrW alloy with fine Cr-rich and W-rich carbides uniformly distributed within the matrix, as shown in Fig. 3(a). Stellite 1 powder had a dendritic microstructure (Fig. 1). The XRD analysis presented in Fig. 4 shows M_6C (Co_3W_3C), M_7C_3 (Cr_7C_3) and $M_{12}C_6$ (Co_6W_6C) carbides along with intermetallic Co_3W and Co. The composition of these carbides is a function of sintering temperature and cooling rates, as discussed in the published literature (Ref 24, 25). The EDS analysis indicated that the approximate composition of the Cr-rich carbide in P1 alloy was $(Cr_{0.76}Co_{0.20}W_{0.04})_7C_3$. The proportion of carbides was a function of high C and Cr, W content in the powder, which resulted in 27.5 ± 1.2% Cr-rich and 13.3 ± 2.5% W-rich carbides (Table 4). Table 6 compares the atomic % ratios of alloying elements with carbon for the alloys. Given the abundance of carbide formers (Cr, W) present in P1 and a reasonably high proportion of C and bearing in mind that the M/C ratio is 3.32 (Table 6), it is unlikely that there would be any uncombined carbon remaining to be a constituent of solid solution matrix. Therefore, the matrix comprises Co and Co_3W (Fig. 4).

The microstructure of Stellite 21 (P3) has been discussed in an earlier publication; hence, only a summary is provided here (Ref 22). The low proportion of C in P3 (Table 1) predominantly resulted in a CoCrMo solid solution matrix with fine $M_{23}C_6$ and MC carbides (Fig. 4, Table 4). The low fraction of carbides due to low C content can also be observed from the highest M/C ratios in Table 6. The Cr/C ratio is higher than Mo/C, so there is a relatively higher proportion of $Cr_{23}C_6$ (5.1 ± 0.8%) carbides. This also shows that no C will be left to form part of the CoCrMo solid solution. $M_{23}C_6$ carbide had the approximate composition of $(Cr_{0.71}Co_{0.20}Mo_{0.09})_{23}C_6$, which is similar to that was previously reported in the literature (Ref 26). Based on the CoCrMo-C phase diagram (Ref 27), the CoCrMo solid solution matrix is generally FCC at higher temperatures and HCP at room temperature. As discussed later, the lack of carbides also resulted in lower hardness and high Charpy impact energy (Table 5).

Table 4 Area fraction of the individual components in the HIPed Stellite alloys

	Co-rich matrix	Cr-rich carbide	W/Mo-rich carbide
P1 (Stellite 1)	Gray, 59.2 ± 3.4%	Dark, 27.5 ± 1.2%	Light, 13.3 ± 2.5%
P2 (50:50 blend)	Gray, 82.2 ± 1.4%	Dark, 9.0 ± 0.8%	Light, 8.9 ± 0.5%
P3 (Stellite 21)	Gray, 93.3 ± 1.6%	Dark, 5.1 ± 0.8%	Light, 1.7 ± 0.8%

Table 5 Mechanical test results of the HIPed Stellite alloys

	P1	P2	P3
Macro-hardness, HV, 294N	632.6 ± 1.5	493.7 ± 17.9	351.2 ± 2.3
Micro-hardness, HV, 2.94N	686.0 ± 18.5	541.0 ± 52.7	371.8 ± 16.3
UTS, MPa	1175.9 ± 0.3	1115.3 ± 11.6	941.1 ± 23.9
0.1% offset Yield strength, MPa	849.3 ± 26.7	669.4 ± 13.5	510.4 ± 5.2
Young's modulus, GPa	230.4 ± 4.4	241.2 ± 9.4	244.6 ± 5.4
Elongation, %	0.30 ± 0.01	0.76 ± 0.04	6.05 ± 1.68
Unnotched Charpy impact energy, J	14.69 ± 0.78	10.85 ± 1.36	94.46 ± 5.13

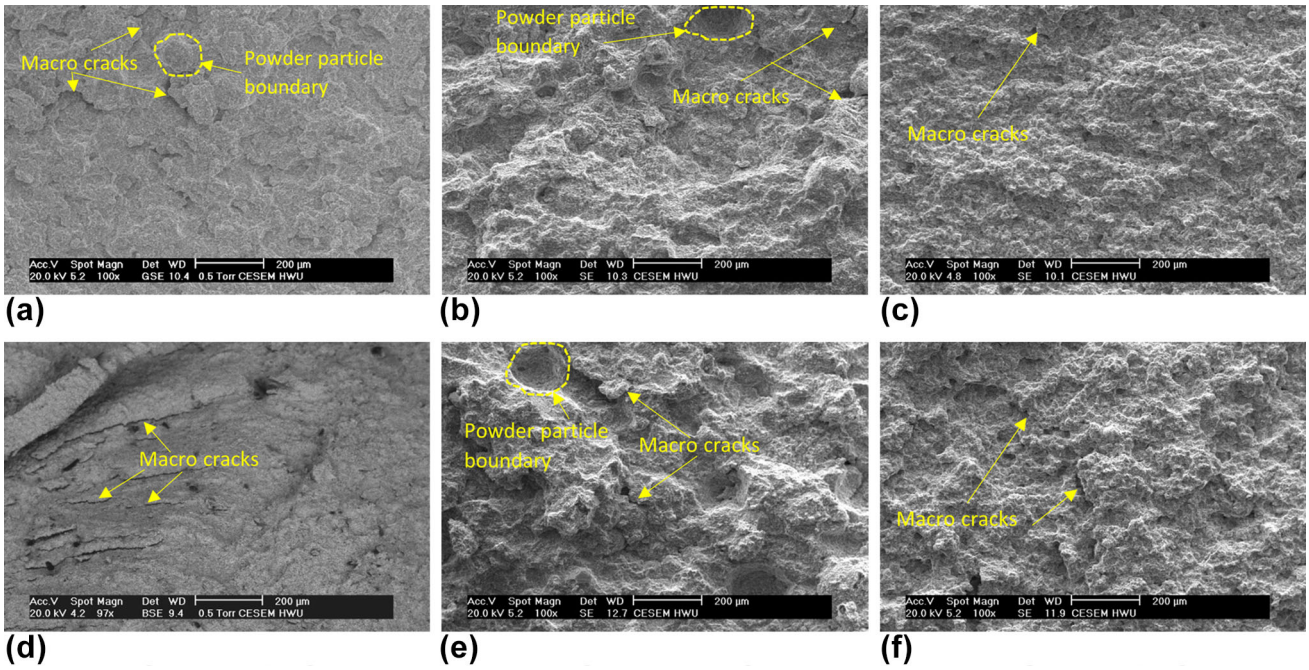

Fig. 5 SEM fractography after the tensile tests on (a) P1, (b) P2, (c) P3, and the Charpy impact tests on (d) P1, (e) P2, (f) P3

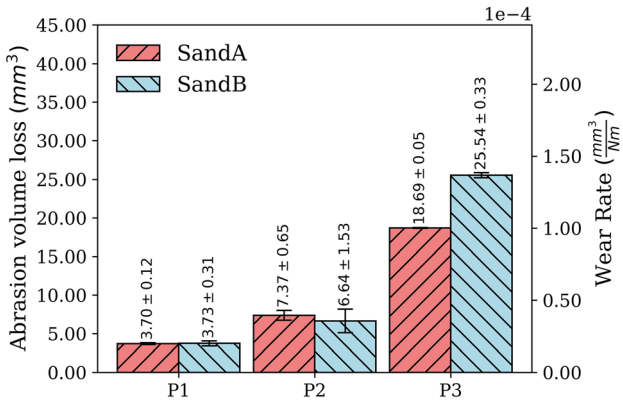

Fig. 6 Volume loss and wear rate for DSRW tests for HIPed Stellite alloys (P1, P2, P3)

The blending of CoCrW (P1) and CoCrMo (P3) alloys resulted in a mixed microstructure in P2. The P1-like region with plenty of W-rich carbides and the P3-like region mainly consisting of Cr-rich carbides coexisted in the blend P2 alloy. Due to the unbalanced carbon contents in the two powders (P1, P3), the carbon atoms diffused from the P1-like region to the P3-like region during the HIPing process. As a result, more Cr-rich carbides (dark phase in Fig. 3b, c) formed in the P3-like region, whereas the carbide density in the P1-like region decreased. Notably, the P1- and P3-like regions were quite different from the P1 and P3 alloys in terms of the carbide type and content, as new carbides formed due to the diffusion of carbon during HIPing (Fig. 3, 4).

XRD analysis (Fig. 4) indicated that the possible components in P1 were α-cobalt (FCC), Co_3W, Cr_7C_3, Co_3W_3C and Co_6W_6C. In P2 and P3, Mo replaced tungsten gradually, and Co_3W_3C was no longer present. Co_7Mo_6 and Co_2Mo_3 began to appear in P2, whereas Co_3W appeared in P1 and P2 only due to the absence of W in P3. Image analysis results (Table 4) showed that due to the difference in the C content of the two powders, the fraction of Cr-rich carbides decreased from 27.5% (P1) to 5.1% (P3). The W-rich carbide (13.3%) in P1 was also replaced by the Mo-rich carbide (1.7% in P3). However, the change in carbide fraction did not follow a linear trend. The total carbide fraction in P2 (17.9%) was lower than the average of P1 and P3 (23.8%). The microstructure of P2 (Fig. 3b, c)

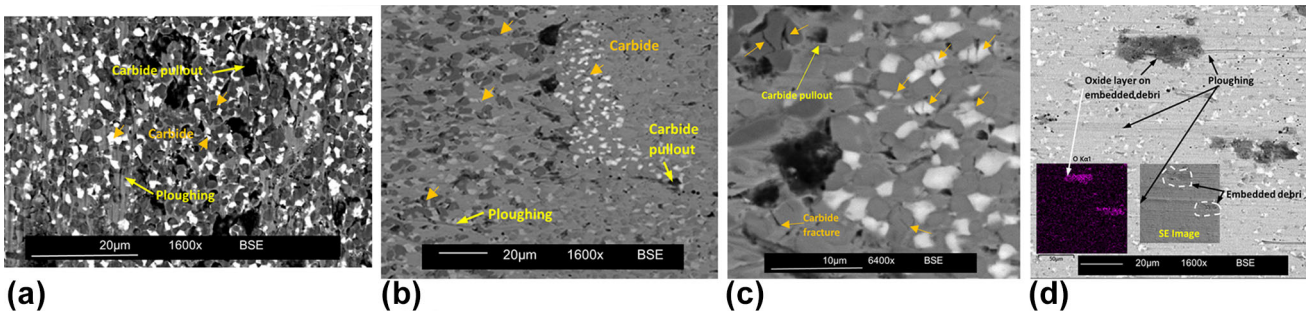

Fig. 7 Wear scars after the DSRW tests on (a) P1 (Stellite 1); (b, c) P2 (blend); (d) P3 (Stellite 21) with EDX Oxygen map and SE image insert

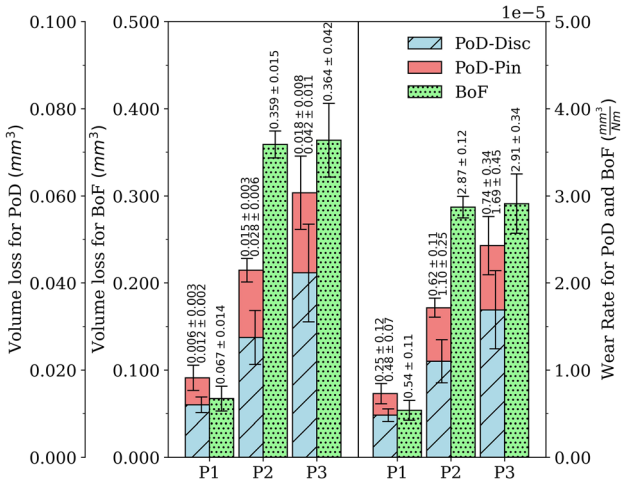

Fig. 8 Volume loss and wear rate for self-mated pin-on-disk (PoD) and ball-on-flat (BoF) test results of HIPed Stellite alloys (P1, P2, P3)

shows that only a few Cr-rich carbides (dark phase) formed in the P1-like region. In comparison with chromium, tungsten seemed to be a preferential carbide former. Therefore, when the alloy's carbon content was limited, the preferential formation of W-rich carbides resulted in decreased Cr-rich carbides in the same region. The Mo content increased from P1 to P3, while the carbon content decreased; therefore, the blended alloy contained higher Mo but lower C. The content of Mo-rich carbide in the P3-like region of the blended alloy was approximately no more than 2%. Most of the carbon in the P3-like region formed Cr-rich carbides.

4.2 Hardness, Tensile and Charpy Impact Toughness

4.2.1 Hardness. Both the macro-hardness and micro-hardness decreased from P1 to P3 (Table 5), indicating that it was due to the variation in the C, W, Cr and Mo content (Table 1), which influenced the carbide fraction (Table 4) and solid solution strengthening of matrix (Fig. 4, Table 5). This analysis of wt.% of C, W and Mo content on the carbide fraction is summarized in Fig. 10(a), which shows a linear relationship between carbon content (C_c) vs. sum of W and Mo (S_{wm}) content. Similarly, there is a near-linear relationship between the total carbide fraction (TCF) and S_{wm}, i.e.,

$$C_c \propto S_{wm} \propto\cong \text{TCF} \qquad \text{(Eq 1)}$$

A comparison of this analysis with an earlier study in (Ref 7) for CoCrW blended alloy of Stellite 6 and Stellite 20 is also summarized in Fig. 10. The current and earlier investigations (Ref 7) show a similar trend as in Eq 1. However, the TCF relationship is not as good for the new CoCrWMo blend as it was for the CoCrW blend in (Ref 7). HIPed Stellite 21 (P3) was the softest alloy mainly because of its lowest carbon and carbide fraction content (Table 1, 4, 5). In most commercially available carbide Stellite alloys, the wt.% content of W, C, Cr and Mo varies from 16.3 to 0, 3.21 to 0.06, 27 to 32 and 12 to 0.5, respectively (Ref 2). However, when seeking a mathematical structure–property relationship between composition and

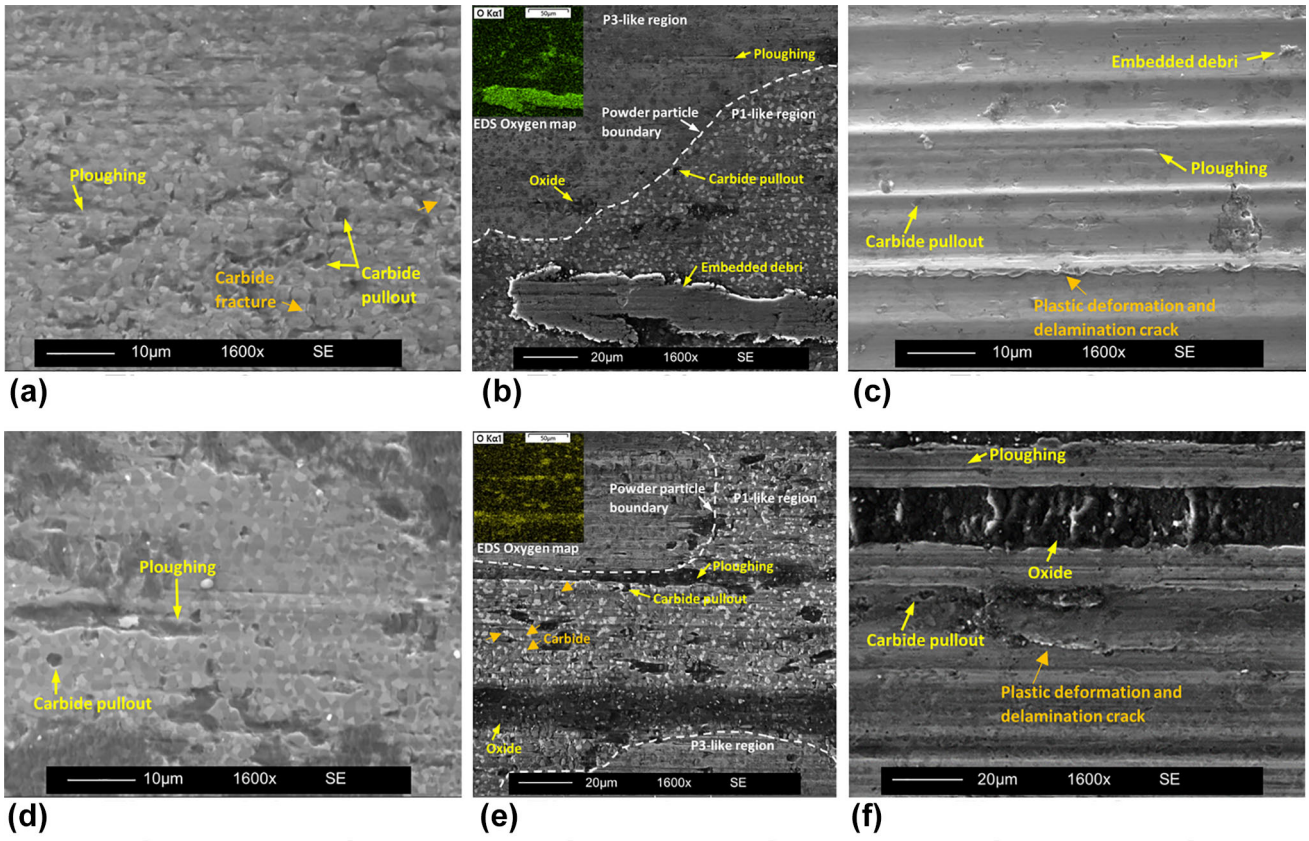

Fig. 9 Wear scars images after the self-mated pin-on-disk tests on the disk sample of (a) P1; (b) P2, (c) P3 and Ball-on-Flat disk (d) P1, (e) P2, (f) P3

Table 6 Chemical compositions and the ratios of alloying elements with carbon for the HIPed alloys (atomic %)

Alloy	Co	Cr	W	Mo	C	Total others	Ratio [Cr + Mo + W]/C	Ratio [Cr]C	Ratio [W + Mo]/C	Ratio [Co + W + Mo + Cr]/C	XRD components detected in HIPed alloy (in decreasing M:C ratio)
P1	44	33.8	3.8	0.17	11.4	6.8	3.32	2.96	0.35	7.2	Co_6W_6C Co_3W_3C Cr_7C_3 Co_3W
P2	50.4	31.9	1.9	1.7	6.4	7.7	5.54	4.98	0.56	13.4	Co_6W_6C Cr_7C_3 Co_3W Co_3Mo Co_2Mo_3 Co_7Mo_6
P3	57	30.1	0	3.2	1.3	8.4	25.4	22.93	2.46	68.8	$Cr_{23}C_6$ MoC Co_3Mo Co_2Mo_3 Co_7Mo_6

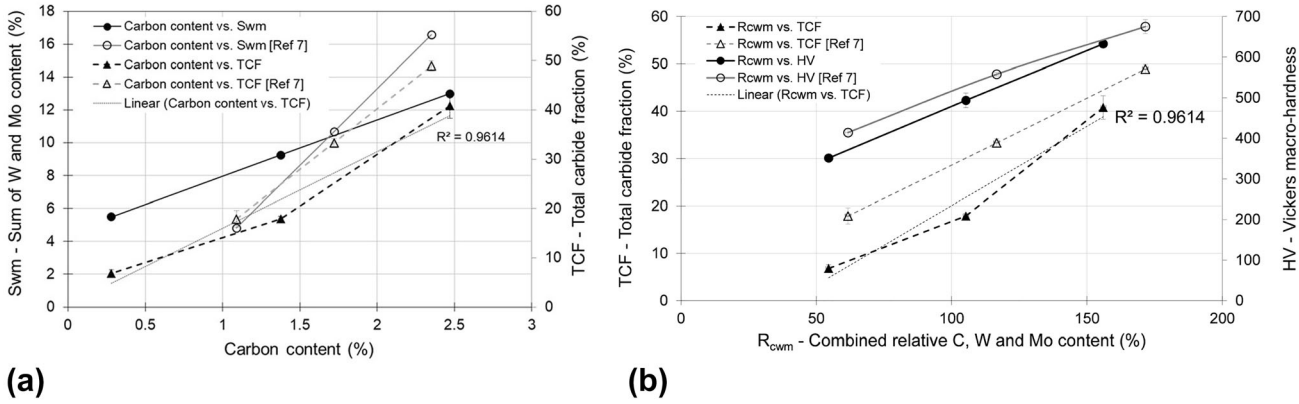

Fig. 10 (a) relationship between C, W, Mo content and total carbide fraction (TCF), (b) relationship between TCF, R_{cmw} and Vickers hardness (HV). Data from (Ref 7) have been readjusted to account for R_{cmw}

hardness, the Cr content can be ignored as it lies within a narrow range of 27–32 wt.%. Similarly, as the wt.% variation between W, C and Mo is significant, a weighted relative combined W, C and M contents (R_{cwm}), based on the maximum values in carbide Stellite alloys (Ref 2), can be used as follows:

$$R_{cwm} = \left(\frac{C_c}{3.21} + \frac{C_w}{16.30} + \frac{C_{Mo}}{12}\right) \times 100 \qquad \text{(Eq 2)}$$

where C_c, C_w and C_{Mo} are the wt.% content of C, W and Mo, respectively. It is worth noting that Eq 2 fundamentally differs from the analysis reported earlier (Ref 7) for wear rate prediction, as it gives equal weight to Mo, based on the composition of the current investigation. Mo was not considered before in the mathematical formulations, so the relationship reported earlier (Ref 7) cannot be applied to the current blend. The analysis based on Eq 2 containing Mo is summarized in Fig. 10(b). This figure shows that the TCF has a linear relationship with R_{cwm} and Vickers hardness. The graph shows this comparison for macro-hardness, which had a similar trend to micro-hardness. However, macro-hardness values are used in this analysis due to the indentation size effect, which averages the hardness value for both the carbides and matrix. Mathematically, this can be expressed as:

$$R_{cwm} \propto TCF \propto \cong HV \qquad \text{(Eq 3)}$$

This new relationship with R_{cmw} also compares well with the earlier investigation of the CoCrW blend (Ref 7), as shown in Fig. 10. Data from (Ref 7) have been readjusted to account for R_{cmw}. Like Eq 1, the TCF relationship is not as good for the new CoCrWMo blend as it was for the CoCrW blend. In summary, the carbon content vs. TCF and R_{cwm} vs. TCF relationship is not an exact fit, whereas carbon content vs. S_{wm} and R_{cwm} vs. HV in Eq 1 and 3, provide an exact fit for both CoCrWMo and CoCrW (Ref 7) alloy blends.

4.2.2 Tensile Test Analysis. HIPed Stellite 1 (P1) had the highest UTS and yield strength due to higher carbide fraction and solid solution strengthening disrupting the dislocation motion (Table 5). The % elongation doubled from P1 and P2 and then increased by an order of magnitude for P3. Figure 10 indicates a linear trend between the carbide fraction and the chemical composition (R_{cwm}). The microstructure of P3 (Fig. 3d) indicates sparse carbides, and hence, the relatively

high ductility of this alloy was dictated by (i) the solid solution matrix instead of carbides, (ii) the absence of W in the solid solution matrix and (iii) the absence of secondary W carbides such as $M_{12}C$, M_6C (Fig. 4, Table 6). Low carbon content in P3 and the absence of W thus resulted in the lowest UTS, yield strength and the highest ductility. The blend P2 had UTS and ductility comparable to P1. However, its yield strength was an average of P1 and P3.

The fractographs of tensile test specimens (Fig. 5a, b, c) show that the carbide/matrix and powder particle boundaries were the main fracture paths. Carbide fracture was not observed in the SEM investigation. P1 powder particle size was between 125 and 45 μm, whereas P3 predominantly ranged around 20μm (Table 2). The powder particle boundaries identified in Fig. 5 are comparable to the P1 particle size. Particle boundaries were not evident in P3, indicating that the dominant fracture path was within the matrix. This is attributed to the relatively smaller powder particle size in P3. In P2, the carbide density in the P1-like region was much higher than that in the P3-like region due to the higher content of tungsten and carbon (Fig. 3b, c). It was, therefore, easier for the cracks to initiate and propagate in the P1-like region. Hence, the UTS and elongation of P2 were more dictated by P1 than P3. There was no significant difference in the values of Young's modulus between the three alloys, and the small differences are attributed to the variations in the chemical composition of these alloys. Figure 11 shows the relationship between yield strength and macro-hardness. The relationship is linear between hardness and inverse of yield strength (σ_y) and can be mathematically expressed as:

$$HV \propto -\sigma_y^{-1} \quad \text{(Eq 4)}$$

which indicates that matrix plasticity instead of carbide fraction dominates the yield strength. Figure 11 also shows that the above relationship can be applied to blends of both the CoCrWMo and CoCrW (Ref 7) alloys.

4.2.3 Charpy Impact Energy. The unnotched Charpy impact energy of HIPed Stellite 21 (P3) was almost an order of magnitude higher than those of P1 and P2 (Table 5). This is consistent with the order of magnitude tensile elongation of P3 compared to P1 and P2. Similar to the fractographs after the tensile tests, the fractographs after the impact tests indicated two main crack propagation routes, the carbide/matrix boundaries and the powder particle boundaries, as shown in Fig. 5(d, e, f). P3 had a very fine microstructure together with very low carbide density. Furthermore, the average powder size of P1 (around 20 μm, Table 2) was much lower than that of P1 (around 120 μm). The fine microstructure and the small powder particle size resulted in a higher density of powder particle boundary, which hindered the propagation of cracks in P3 by disrupting the crack propagation path. The microstructure had a more significant effect on the impact energy than the difference in the powder particle size. This can be observed from an earlier investigation where HIPed P3 was compared with the cast counterpart, and the Charpy impact energy of the HIPed and cast Stellite 21 was 94.5 $\pm$ 5.1 and 125.3 $\pm$ 33.8 J, respectively (Ref 22). Although the cast Stellite 21 showed a higher average value, its standard deviation is also high due to the complex carbide structure. As discussed earlier in Sect. 4.2.2, the presence of a P1-like region with high carbide density in the P2 blend resulted in the formation of macro-cracks and, thus, lower impact energy.

As the results of tensile elongation ($E_{\%}$) and Charpy impact energy (E_c) showed a similar trend, the analysis in Fig. 11 shows a linear relationship between them. However, the relationship between E% and E_c does not provide a good fit at lower values of both variables, as indicated by the dotted circle in Fig. 11. This also shows that matrix ductility dominates both E_c and $E_{\%}$. However, the relationship cannot predict the trend of elongation vs. impact energy at lower values of J for the new CoCrWMo alloy blend.

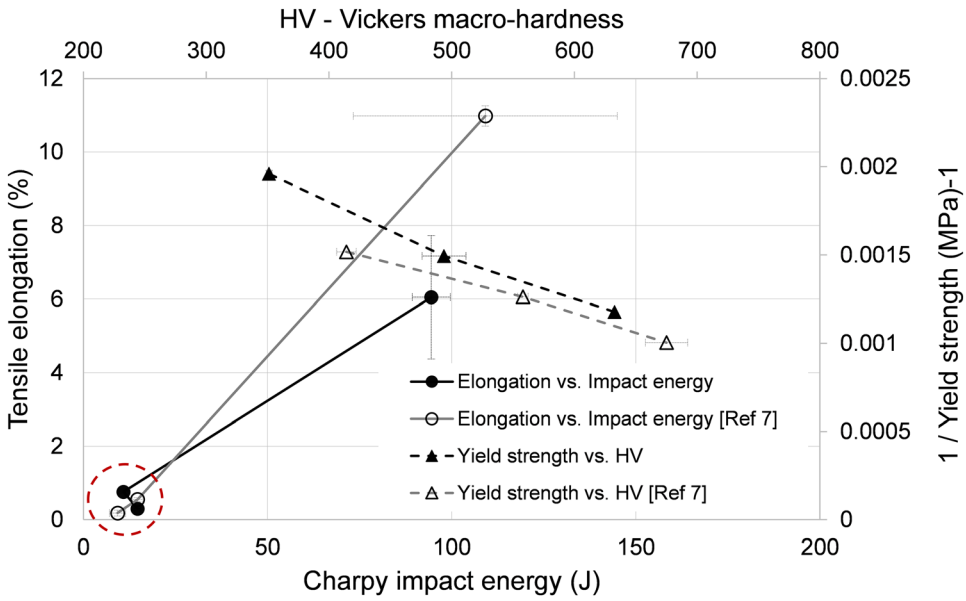

Fig. 11 Relationship between (i) tensile elongation ($E_{\%}$) and Charpy impact energy (E_c), (ii) Vickers hardness (HV) and yield strength (σ_y)

4.3 Wear Performance

4.3.1 Abrasive Wear. DSRW results summarized in Fig. 6 showed that HIPed Stellite 1 (P1) had the best abrasive wear resistance, almost twice that of P2. HIPed Stellite 21 (P3) showed a ~ 500% decrease in wear resistance compared to P1. The DSRW abrasive wear rate was similar for both sands in P1 and P2, whereas it was lower by ∽ 36% for Sand A in P3. This difference in the wear rate for sand A and B in P3 is attributed to its lower TCF, where the soft matrix eroded more with coarse sand B, as the lower proportion of carbides did not provide resistance to plowing. This difference in wear rate was less in P1 and P2 due to the influence of carbides, which reduced the matrix area and provided a discontinuity during plowing by the sand particles, as shown in Fig. 7.

SEM investigation of the wear scars in Fig. 7 shows that the abrasive wear was dominated by carbide fracture, carbide pullout and plowing of the metal matrix. These wear mechanisms are consistent with earlier findings of Stellite alloys, indicating a dependence of the wear mechanism on carbide size, shape, matrix composition and hardness of the abrasive media (Ref 2, 12, 28, 29). Desai et al. (Ref 29) investigated the influence of carbide size on the abrasion resistance of Stellite alloys. They concluded that micro-machining of the softer metal matrix by the abrasive particles leads to carbide pullout. The abrasive particles can also cut larger carbides. Cobalt also undergoes face-centered cubic (FCC) to hexagon close-packed (HCP) transformation under strain, which further influences the wear mechanism (Ref 1, 2). This transformation is due to the low stacking fault energy (SFE) of FCC cobalt, which improves the wear properties of Stellite alloys, as discussed by Woodford et al. (Ref 30) and Bhansali et al. (Ref 31). The abrasive sand particles can also fracture carbides under contact stress. As the abrasive particles roll and slide past the carbides during the DSRW tests, Yu et al. (Ref 32) have shown that the Hertzian contact stress under these contact conditions can reach 5GPa, resulting in carbide fracture.

For P1, carbide pullout and fracture were the dominant abrasive wear modes (Fig. 7a). There was some evidence of plowing through the matrix. However, P1 had ~ 41% carbide fraction, which provided resistance to plowing through the matrix. This is consistent with the findings of other high-C and high-W Stellite alloys, such as Stellite 20 (Ref 32). The abrasive wear mechanism of P3 was dominated by plowing of the matrix, leading to material loss. This was due to the significantly low carbide fraction in (~7%) P3 (Table 4).

In some cases, the finer carbides in P3 were also removed in this process (Fig. 7d). There was evidence of oxidized embedded debris in the wear track of P3, as shown by the SE image insert in Fig. 7(d). The EDS analysis confirmed the debris oxidation, as indicated by the insert in Fig. 7(d). The embedding of debris is attributed to the large proportion of softer matrix providing sites for debris entrapment due to lower carbide fraction. As shown later, the debris entrapment for the alloy containing P3 was also observed in sliding wear tests (Fig. 9b). The oxidation observed in P3 is likely due to the formation of MoO_x oxide film in alloys containing Mo, which is consistent with the findings of Tan et al. (Ref 33). They observed this oxide film as predominantly MoO_3.

SEM observation of P2 (Fig. 7b, c) indicated a combination of carbide fracture and carbide pullout in the P1-like region and plowing in the P3-like region. The carbide fracture was observed in both W-rich $M_{12}C$ and Cr-rich M_7C3 carbides (Table 6, Fig. 7c). Noting that the powder particle size of P3 (Table 2) was ~ 7 times smaller than the P1 powder, the plowing through P3-like region was limited due to disruption of the plowing path by higher-carbide P1-like region. As discussed earlier in section 4.1, diffusion of carbon led to changes in carbide components in P2. Both factors, i.e., i) changes in the chemical composition of P1 and P3-like regions and ii) difference in powder particle size, resulted in the DSRW wear rate performance, which was dominated by higher-carbide density P1-like region (Fig. 6).

The structure–property relationship of the averaged abrasive wear rate (W_{DSRW}) is summarized in Fig. 12. Unlike the previous investigation of the blended CoCrW alloys (Ref 7), the significant variation in the chemical composition of P1 and P3 does not result in a linear relationship between W_{DSRW} and TCF. Hence, the relationship of $\Delta W_{DSRW} \propto - \Delta_{Rcw} \propto - \Delta TCF \propto HV$ reported in (Ref 7) for the CoCrW alloy blend cannot be applied to the current CoCrWMo blend. The DSRW wear rate for the current alloy blend was more sensitive to TCF than hardness (Eq 4). However, given that the wear mechanism is dominated by the plowing of the soft matrix in P3 and the high proportion and hardness of carbides in P2 and P3, Fig. 12 shows a linear relationship between W_{DSRW} and Log (HV). As the DSRW wear mechanism was also influenced by carbide fracture, a better relationship exists with Log $\left(\frac{TCF \times HV}{E_c}\right)$, as shown in Fig. 12. Mathematically, the wear rate of DSRW (W_{DSRW}) can be expressed as:

$$W_{DSRW} \propto \cong \mathrm{Log}(HV) \propto \mathrm{Log}\left(\frac{TCF \times HV}{E_c}\right) \qquad \text{(Eq 5)}$$

The above relationship was not explored in (Ref 7) and has also been applied to evaluate its suitability for the blended CoCrW alloys, as shown in Fig. 12.

4.3.2 Pin-on-Disk Sliding Wear. Unlike the DSRW results, the self-mated PoD wear rate showed a near-linear trend with HV (Fig. 8 and Table 5). Although there was still a significant difference in the wear resistance of P1 and P3, P2 performance was an average of the wear rate of the base alloys (P1, P2), after considering the carbide fraction and HV. The SEM observations of the wear tracks in Fig. 9(a, b, c) indicate that carbide pullout, fracture and plowing were the main wear mechanisms. For P1, carbide fracture and pullout dominated wear due to high carbide density and hardness. There was also evidence of plowing by surface asperities in the contact region interrupted by carbides. There was some evidence of oxide film in the wear track, which is attributed to the formation of WO_x. The asperity interaction during dry sliding wear can result in flash temperatures reaching several hundred degrees, resulting in the oxidized film formed by the oxidation of elemental species in the contact system (Ref 34). These oxidized films can reduce the friction and wear of the contact pair. Engqvist et al. investigated the formation of WO_x tribofilm during the sliding wear of WC-cemented carbides and showed that the oxidized tribofilm has the composition of WO_3 (Ref 35). Their investigation also showed that Co does not readily oxidize during sliding wear. The exact composition of the oxidized film was not investigated in the current work, but this film formation is consistent with earlier studies (Ref 2, 7).

Plowing, carbide pullout and repeated cycles of plastic deformation leading to delamination cracks dominated the wear mechanism of P3 (Ref 36). There was also evidence of

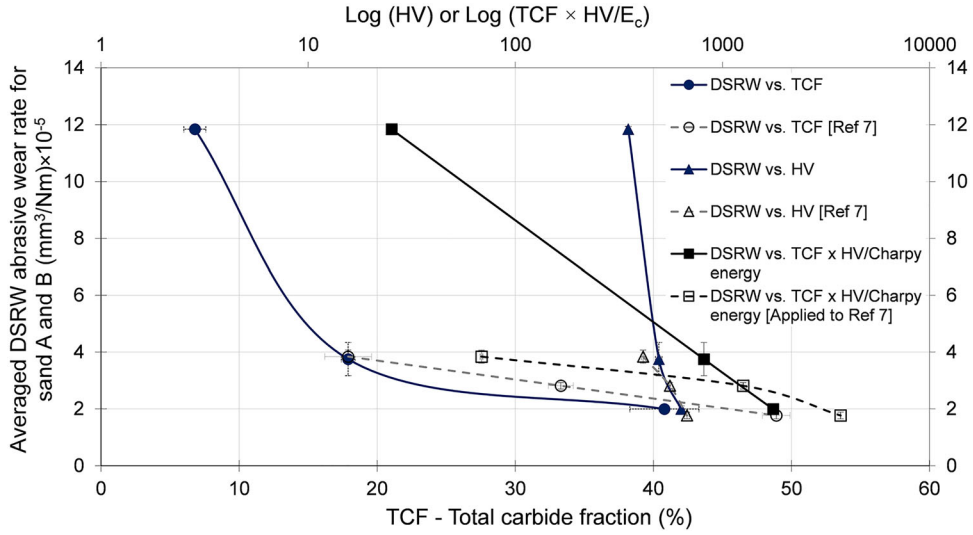

Fig. 12 Relationship between DSRW wear rate and (i) TCF, (ii) Log (HV) and (iii) Log (TCF × HV/E_c)

embedded debris in P3 (Fig. 9c), which is consistent with the wear track observations of this alloy in DSRW tests (Fig. 7d). Hence, plastic deformation dominates the P3 wear mechanism.

SEM observation of P2 showed plowing and oxidation in the P3-like region and carbide fracture and pullout in the P1-like region (Fig. 9b). A large oxidized debris of the P3-like region can also be seen embedded in the P1-like region of P2. Hence, there was adhesion of a P3-like region in the sliding wear process. There is also some evidence of oxidation in the P1-like region, as shown by the EDS oxygen map insert in Fig. 9b. Delamination cracks can also be observed on the embedded debris. The oxidation in the P3-like region is likely due to MoO_x, further details of which can be seen in research published by Tan et al. (Ref 33). The composition of this oxidized film was not further investigated in the current work. The oxidation in the P1-like region is likely to be WO_x (Ref 35). Taufiqurrakhman et al. (Ref 37) have investigated the influence of tribocorrosion and surface tribofilms in CoCrMo Stellite alloys under a boundary lubrication system.

In terms of the structure–property relationship, taking into consideration the sliding wear mechanism of fracture and plastic deformation, the CoCrWMo blend does not follow the earlier reported relationship of $W_{PoD} \propto (1/R_{cw})^2 \propto (1/TCF)^2 \propto (1/HV)^3$ for CoCrW blend (Ref 7). Hence, new mathematical relationships need to be explored, which can be applied to both CoCrW and CoCrWMo alloy blends. Figure 13 summarizes such a relationship and shows a near-linear behavior with $\left(\frac{TCF \times HV}{E_c}\right)$. This relationship of wear rate is the same as equation (5), albeit without the log scale. Mathematically, the wear rate for PoD (W_{PoD}) can be expressed as:

$$W_{PoD} \propto \cong (HV) \propto \left(\frac{TCF \times HV}{E_c}\right) \quad \text{(Eq 6)}$$

The above equation also fits the CoCrW blend and is applied to (Ref 7) on a log scale (Fig. 13).

4.3.3 Ball-on-Flat Sliding Wear. A comparison of wear rates in Fig. 6 and 8 shows a significant difference in the wear rate of P1 and P3. This difference shows the sensitivity of wear mechanism changes between DSRW and BoF, resulting in a P2 wear rate similar to P3 for the latter. Contrary to this, the P2 wear rate was comparable to P1 in the DSRW tests, whereas it was an average of P1 and P3 for the PoD. The wear rate for the BoF in P2 was very similar to P3 (Fig. 8), indicating that the P3-like region in this blend dominated the performance. This is attributed to the changes in the following tribological test conditions.

1. The contact pressure at the start of the BoF test (Table 3) was almost twice that of PoD. As there was negligible wear in the ball, the contact stress remains high compared to PoD, where the pin material wears to reduce stress as the contact conforms. The wear debris entrapment in the wear track also influenced the stress distribution.
2. The Vickers hardness of the sintered WC-Co ball was 1633 (manufacturer's data) was ∽3.3 times that of P2 and ∽4.5 times that of P3. Hence, the hardness of the WC-Co ball dominated the wear mechanism. This hardness difference also existed for the DSRW tests, where the hardness of the Silica sand can be approximated as 13 GPa (Ref 38); however, the sand particles can fracture under contact stress as their fracture toughness (∽1.4 MPa $(m)^{1/2}$) (Ref 38) is almost an order of magnitude less than that of sintered WC-Co (∽10 to 15 MPa $(m)^{1/2}$) (Ref 39). Therefore, both the higher hardness and fracture toughness of the WC-Co ball dominated the wear of the P3-like region in P2.
3. A comparison of the SEM observations in Fig. 9 shows that plowing was significant in both P1 and P1-like regions in P2, which was more severe when compared to the PoD test. This is partly due to the longer sliding distance in BoF (Table 3) and partly due to the harder WC-Co counterbody. Therefore, there is more significant wear in both P1-like and P3-like regions of P2, which is attributed to the presence of carbides in the wear debris accelerating the wear process compared to PoD tests, where the P1-like region shows relatively less significant wear.
4. There is an oxide layer in all the SEM observations of the BoF test, which is attributed to the presence of W as the counterbody leading to WO_x film along with a potential contribution from MoO_x as discussed earlier (Ref 33,

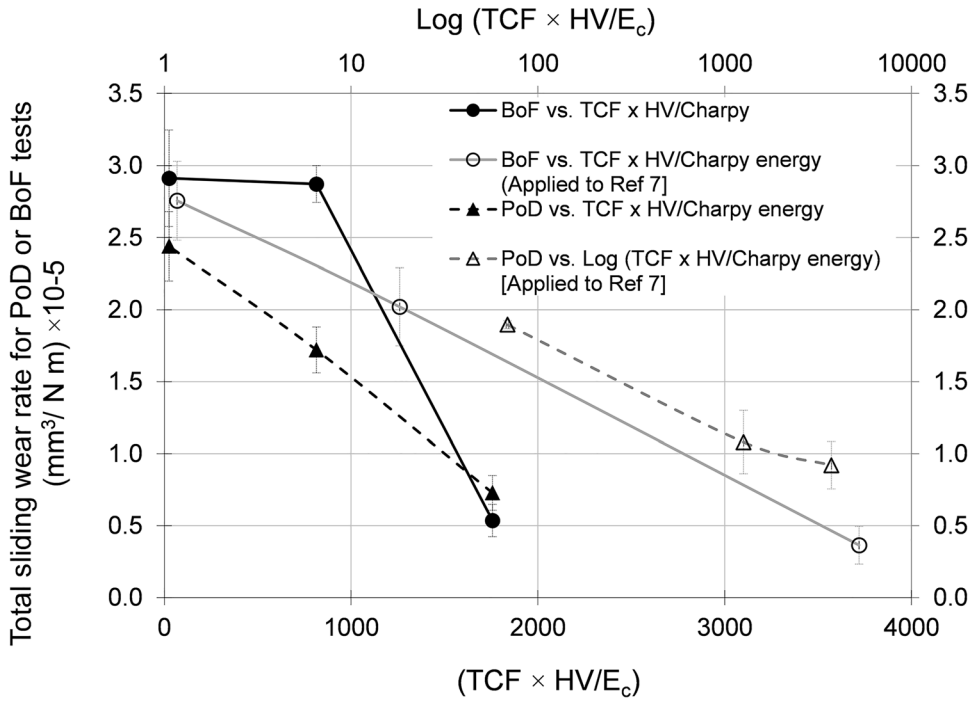

Fig. 13 Relationship between PoD and BoF wear rate and (i) (TCF × HV/E_c), (ii) Log (TCF × HV/E_c)

35) and consistent with the findings in earlier studies (Ref 7, 39).

In terms of the structure–property relationship, as summarized in Fig. 13, the BoF wear rate did not show a trend with either TCF, HV, E_c or a combination of these factors. The BoF results of the CoCrW alloy blend in (Ref 7), however, show the same dependency of wear rate on $\left(\frac{TCF \times HV}{E_c}\right)$ as summarized in Eq 6 and Fig. 13.

4.3.4 Opportunities for Machine Learning. Machine learning (ML) is becoming more critical in decreasing the experimental cost associated with alloy development and tailoring the alloy design for structure–property relationships for specific applications. A recent review by Hu et al. (Ref 40) has shown that growing efforts have been devoted to integrating ML with alloy design. This data-driven method has shown promising outcomes in inferring from alloy features (e.g., elemental compositions) to targets of interest (e.g., mechanical properties). This process, known as forward prediction, speeds up the design process. This process also significantly reduces the cost of alloy development by benchmarking specific alloy compositions likely to yield properties for particular applications. These concepts are already being realized in industry, e.g., in the FORGE project, which aims to provide a new knowledge-based framework to design tailored compositionally complex materials (CCMs, both alloys and ceramics) with the required combination of hardness, smoothness, toughness, gas impermeability and/or corrosion resistance tailored to meet the specific future and current needs in an energy-intensive processing environment (Ref 20). Alloy composition can be achieved through casting, coatings, powder metallurgy manufacturing and 3D printing; however, the atomization process for powder manufacture can limit the variations in alloy design. Blending standard powders through mechanical alloying can overcome this by allowing two or more powders to be combined (Ref 41). This can provide a cost-effective solution to alloy development.

Mathematical models based on the structure–property relationship are also critical in guiding ML alloy development. Current and past research in this area can provide crucial data for ML alloy development for engineering applications. These models can account for changes in microstructure caused by the alloy manufacturing route; for example, in tribomechanical applications, the carbide size and shape can alter the properties of the same alloy composition (Ref 4). As more data become available, these models will inevitably guide future alloy developments through ML. Future investigations to include other alloy compositions in addition to the 50:50 blend in the current work and opportunities to blend other Stellite alloys not considered in published research can provide valuable data for ML.

5. Conclusions

Two different wear-resistant Stellite alloys, high-carbon and high-tungsten CoCrW (Stellite 1, P1) and low-carbon, high-molybdenum CoCrMo (Stellite 21, P3), were blended to make a new CoCrWMo (P2) alloy via HIP consolidation. New mathematical relationships that apply to both CoCrW and CoCrWMo alloy blends are developed. Tribomechanical and Structure–property relationships are summarized below.

1. The blended alloy's microstructure resulted from carbon diffusion from a high-concentration P1-like region to P3. $M_{12}C$ and M_7C_3 carbides from P1 were retained in P2, whereas M_6C was not observed in P2. Similarly, MoC was not observed in P2, indicating that Mo formed part of the matrix in P2.

2. The wear mechanism of DSRW tests showed carbide fracture and pullout as the dominant mechanisms for P1 and P2, whereas P3 predominantly showed plowing and embedded oxidized debris. The wear rate of P2 was more like P1, indicating that carbides and intermetallics in the blended alloy dominated the wear mechanism.
3. The wear rate of DSRW showed a complex relationship with HV, TCF and E_c, i.e., $W_{DSRW} \propto\cong \text{Log}(HV) \propto \text{Log}\left(\frac{TCF\times HV}{E_c}\right)$ (Eq 5). While the previously reported proportional relationship of $W_{DSRW} \propto$ - Rcw $\propto$ - TCF $\propto$ HV only applies to the CoCrW alloy blend, Eq 5 can be applied to both CoCrW and CoCrWMo blends.
4. Self-mated PoD tests showed a wear mechanism similar to DSRW tests with more evidence of oxidized embedded debris. On average, the wear rate of P2 was between P1 and P3, indicating that both CoCrW- and CoCrMo-like regions contributed equally to the wear resistance. PoD wear resistance was linked to TCF, HV and E_c using the relationship $W_{PoD} \propto\cong (HV) \propto \left(\frac{TCF\times HV}{E_c}\right)$ (Eq 7). This relationship applies well to both CoCrW and CoCrWMo alloy blends.
5. The higher hardness and toughness of the sintered WC-Co ball dominated the wear of BoF tests. There was more significant evidence of oxidation in all cases due to WO_x and MoO_x. The wear resistance of the blended alloy P2 was similar to P3, indicating that the softer P3-like region dominated the wear mechanism against the harder WC-Co ball. The relationship between the BoF wear rate and TCF, HV and E_c was more complex. No mathematical relationship could satisfy the BoF performance of both CoCrW and CoCrWMo blends.

Acknowledgment

The authors would like to acknowledge the contribution of Dr Hao Yu for the experimental work. The authors also acknowledge the support of Deloro Stellite UK and Bodycote HIP UK for the preparation of test samples used in this investigation.

Open Access

References

1. P. Crook, Cobalt-Base Alloys Resist Wear, Corrosion, and Heat, *Adv. Mater. Process.*, 1994, **145**(4), p 27–30
2. R. Ahmed and H. de Villiers-Lovelock, *Friction and Wear of Cobalt-Base Alloys*, ASM International, 2017. https://doi.org/10.31399/asm.hb.v18.a0006390
3. R. Liu, X.J. Wu, S. Kapoor, M.X. Yao, and R. Collier, Effects of Temperature on the Hardness and Wear Resistance of High-Tungsten Stellite Alloys, *Metall. Mater. Trans. A*, 2015, **46**(2), p 587–599. https://doi.org/10.1007/s11661-014-2664-8
4. H. Yu, R. Ahmed, H. de Villiers Lovelock, and S. Davies, Influence of Manufacturing Process and Alloying Element Content on the Tribomechanical Properties of Cobalt-Based Alloys, *J. Tribol.*, 2008 https://doi.org/10.1115/1.2991122
5. R. Ahmed, H.L. de Villiers Lovelock, S. Davies, and N.H. Faisal, Influence of Re-HIPing on the Structure–Property Relationships of Cobalt-Based Alloys, *Tribol. Int.*, 2013, **57**, p 8–21. https://doi.org/10.1016/j.triboint.2012.06.025
6. S.I. Hango, L.A. Cornish, L.H. Chown, J.W. van der Merwe, and F.P.L. Kavishe, Sliding Wear Resistance of the Cobalt-Based Coatings, ULTIMETTM and STELLITETM 6 with Ruthenium Additions, *Eng. Fail. Anal.*, 2024, **155**, 107717. https://doi.org/10.1016/j.engfailanal.2023.107717
7. R. Ahmed, H.L. de Villiers Lovelock, and S. Davies, Sliding Wear of Blended Cobalt Based Alloys, *Wear*, 2021 https://doi.org/10.1016/j.wear.2020.203533
8. S.P. Kakade, A.G. Thakur, D.D. Deshmukh, and S.B. Patil, Experimental Investigations and Optimisation of Ni-Cr-B-Si Hardfacing Characteristics Deposited by PTAW Process on SS 410 Using Response Surface Method, *Adv. Mater. Process. Technol. Taylor Francis*, 2023, **9**(3), p 826–842. https://doi.org/10.1080/2374068X.2022.2097420
9. K. Song, C. Liu, M. Chen, L. Xie, W. Sun, and F. Wang, Effect of Si Addition on Microstructures and Oxidation Behavior of CoCrW Alloy Prepared by Spark Plasma Sintering, *Corros. Sci.*, 2023, **214**, 111011. https://doi.org/10.1016/j.corsci.2023.111011
10. X. Yang, C. Li, M. Zhang, Z. Ye, X. Zhang, M. Zheng, J. Gu, J. Li, and S. Li, Dry Sliding Wear Behavior of Additively Manufactured CoCrWNixAly Alloys, *Wear*, 2022, **496–497**, 204285. https://doi.org/10.1016/j.wear.2022.204285
11. R. Collier, X. Zhang, R. Liu, X. Wu, and M. Yao, Tribological Performance of Molybdenum Stellite Alloys under Dry-Sliding Wear, *J. Materi. Eng. Perform.*, 2020, **29**(2), p 1384–1399. https://doi.org/10.1007/s11665-020-04650-y
12. R. Ahmed, A. Ashraf, M. Elameen, N.H. Faisal, A.M. El-Sherik, Y.O. Elakwah, and M.F.A. Goosen, Single Asperity Nanoscratch Behaviour of HIPed and Cast Stellite 6 Alloys, *Wear*, 2014, **312**(1), p 70–82. https://doi.org/10.1016/j.wear.2014.02.006
13. S.R. Karthik, N.V. Londe, R. Shetty, R. Nayak, and A. Hedge, Optimization and Prediction of Hardness, Wear and Surface Roughness on Age Hardened stellite 6 alloys, *Manuf. Rev.*, 2022, **9**, p 10. https://doi.org/10.1051/mfreview/2022008
14. M. Sebastiani, V. Mangione, D. De Felicis, E. Bemporad, and F. Carassiti, Wear Mechanisms and In-Service Surface Modifications of a Stellite 6B Co-Cr Alloy, *Wear*, 2012, **290–291**, p 10–17. https://doi.org/10.21825/scad.v4i2.1039
15. V.L. Ratia, D. Zhang, M.J. Carrington, J.L. Daure, D.G. McCartney, P.H. Shipway, and D.A. Stewart, Comparison of the Sliding Wear Behaviour of Self-Mated HIPed Stellite 3 and Stellite 6 in a Simulated PWR Water Environment, *Wear*, 2019, **426–427**, p 1222–1232. https://doi.org/10.1016/j.wear.2019.01.116
16. W. Gao, Y. Lian, G. Xie, J. Huang, L. Zhang, M. Ma, C. Zhao, Z. Zhang, K. Liu, S. Zhang, and J. Zhang, Study of Dry Sliding Wear Characteristics of Stellite 6B versus AISI M2 Steel at Various Sliding Velocities, *Wear*, 2018, **402–403**, p 169–178. https://doi.org/10.1016/j.wear.2018.02.015
17. X.-G. Yue, G. Zhang, Q. Wu, F. Li, X.-F. Chen, G.-F. Ren, and M. Li, Wearing Prediction of Stellite Alloys Based on Opposite Degree Algorithm, *Rare Met.*, 2015, **34**(2), p 125–132. https://doi.org/10.1007/s12598-014-0430-0
18. M.A. Ashraf, R. Ahmed, O. Ali, N.H. Faisal, A.M. El-Sherik, and M.F.A. Goosen, Finite Element Modeling of Sliding Wear in a Composite Alloy Using a Free-Mesh, *J. Tribol.*, 2015 https://doi.org/10.1115/1.4029998
19. R. Ahmed, A. Fardan, and S. Davies, Mapping the Mechanical Properties of Cobalt-Based Stellite Alloys Manufactured via Blending, *Adv. Mater. Process. Technol.*, 2023 https://doi.org/10.1080/2374068X.2023.2220242

20. FORGE: Novel Coatings for Sustainable Industrial Future, n.d., https://www.twi-global.com/media-and-events/press-releases/2020/forge-novel-coatings-for-sustainable-industrial-future. Accessed 17 November 2024
21. R. Liu, J. Yao, Q. Zhang, M.X. Yao, and R. Collier, Effects of Molybdenum Content on the Wear/Erosion and Corrosion Performance of Low-Carbon Stellite Alloys, *Mater. Des.*, 2015, **78**, p 95–106. https://doi.org/10.1016/j.matdes.2015.04.030
22. R. Ahmed, H.L. de Villiers Lovelock, N.H. Faisal, and S. Davies, Structure–Property Relationships in a CoCrMo Alloy at Micro and Nano-Scales, *Tribol. Int.*, 2014, **80**, p 98–114. https://doi.org/10.1016/j.triboint.2014.06.015
23. I. Radu, D.Y. Li, and R. Llewellyn, Tribological Behavior of Stellite 21 Modified with Yttrium, *Wear*, 2004, **257**(11), p 1154–1166. https://doi.org/10.1016/j.wear.2004.07.013
24. M.A. Ashworth, M.H. Jacobs, and S. Davies, Microstructure and Property Relationships in Hipped Stellite Powders, *Powder Metall. SAGE Publ.*, 1999, **42**(3), p 243–249. https://doi.org/10.1179/003258999665585
25. P.J. Mcginn, P. Kumar, A.E. Miller, and A.J. Hickl, Carbide Composition Change during Liquid Phase Sintering of a Wear Resistant Alloy, *Metall. Trans. A*, 1984, **15**(6), p 1099–1102. https://doi.org/10.1007/BF02644703
26. A.J.T. Clemow and B.L. Daniell, Solution Treatment Behavior of Co-Cr-Mo Alloy, *J. Biomed. Mater. Res.*, 1979, **13**(2), p 265–279. https://doi.org/10.1002/JBM.820130208
27. W.V. Youdelis and O. Kwon, Carbide Phases in Cobalt Base Superalloy: Role of Nucleation Entropy in Refinement, *Metal Sci.*, 1983, **17**(8), p 379–384. https://doi.org/10.1179/030634583790420664
28. T.H. Kosel, S.Z. Li, and C.M. Rao, The Size Effect in Abrasion of Dual-Phase Alloys, *A S L E Trans.*, 1985, **28**(3), p 343–350. https://doi.org/10.1080/05698198508981629
29. V.M. Desai, C.M. Rao, T.H. Kosel, and N.F. Fiore, Effect of Carbide Size on the Abrasion of Cobalt-Base Powder Metallurgy Alloys, *Wear*, 1984, **94**(1), p 89–101. https://doi.org/10.1016/0043-1648(84)90168-6
30. D.A. Woodford, Cavitation-Erosion-Lnduced Phase Transformations in Alloys, *Metall. Trans.*, 1972, **3**(5), p 1137–1145. https://doi.org/10.1007/BF02642445
31. K.J. Bhansali and A.E. Miller, The Role of Stacking Fault Energy on Galling and Wear Behavior, *Wear*, 1982, **75**(2), p 241–252. https://doi.org/10.1016/0043-1648(82)90151-X
32. H. Yu, R. Ahmed, and H. de Villiers Lovelock, A Comparison of the Tribo-Mechanical Properties of a Wear Resistant Cobalt-Based Alloy Produced by Different Manufacturing Processes, *J. Tribol.*, 2007, **129**(3), p 586–594. https://doi.org/10.1115/1.2736450
33. H. Tan, Q. Sun, J. Chen, S. Zhu, J. Cheng, and J. Yang, Dry Sliding Tribological Properties and Wear Mechanisms of Mo-Si-B-xTi Alloys at the Temperature Range of 25–1000 °C, *Tribol. Int.*, 2023, **177**, 107897. https://doi.org/10.1016/j.triboint.2022.107897
34. J. Glascott, F.H. Stott, and G.C. Wood, The Effectiveness of Oxides in Reducing Sliding Wear of Alloys, *Oxid. Met.*, 1985, **24**(3), p 99–114. https://doi.org/10.1007/BF00664227
35. H. Engqvist, H. Högberg, G.A. Botton, S. Ederyd, and N. Axén, Tribofilm Formation on Cemented Carbides in Dry Sliding Conformal Contact, *Wear*, 2000, **239**(2), p 219–228. https://doi.org/10.1016/S0043-1648(00)00315-X
36. S. Jahanmir, N.P. Suh, and E.P. Abrahamson, The Delamination Theory of Wear and the Wear of a Composite Surface, *Wear*, 1975, **32**(1), p 33–49. https://doi.org/10.1016/0043-1648(75)90203-3
37. M. Taufiqurrakhman, A. Neville, and M.G. Bryant, The Effect of Protein Structure and Concentration on Tribocorrosion and Film Formation on CoCrMo Alloys, *J. Bio. Tribo. Corros.*, 2021, **7**(4), p 147. https://doi.org/10.1007/s40735-021-00585-6
38. C. Bousbaa, M.A. Madjoubi, Z. Hamidouche, and N. Bouaouadja, Effect of Sand Blasting on Soda Lime Glass Properties, 2003, **16**
39. R. Ahmed, O. Ali, C.C. Berndt, and A. Fardan, Sliding Wear of Conventional and Suspension Sprayed Nanocomposite WC-Co Coatings: An Invited Review, *J. Therm. Spray. Tech.*, 2021, **30**(4), p 800–861. https://doi.org/10.1007/s11666-021-01185-z
40. M. Hu, Q. Tan, R. Knibbe, M. Xu, B. Jiang, S. Wang, X. Li, and M.-X. Zhang, Recent Applications of Machine Learning in Alloy Design: A Review, *Mater. Sci. Eng. R. Rep.*, 2023, **155**, 100746. https://doi.org/10.1016/j.mser.2023.100746
41. J.S. Benjamin, Mechanical Alloying, *Sci. Am. Divis. Nat. Am. Inc.*, 1976, **234**(5), p 40–49. https://doi.org/10.1038/scientificamerican0576-40